Journal of Aircraft
Vol. 56, No. 2, March–April 2019

Roll Control of Low-Aspect-Ratio Wings Using Articulated Winglet Control Surfaces

Richard O'Donnell* and Kamran Mohseni†
University of Florida, Gainesville, Florida 32611

DOI: 10.2514/1.C034704

The use of tip mounted winglets with independently variable cant angles was investigated as a means of roll control on wings with an aspect ratio of one. Wind-tunnel testing was performed in which a six-axis force balance was used to measure the total aerodynamic load on wings with winglet control surfaces. Stereoscopic digital particle image velocimetry of the near-wake plane was used to show how the topology of the tip vortices changed with winglet deflection. Shifts in the location of the right tip vortex core are considered to be responsible for roll moment generation because they indicate changes in the symmetry of suction-side flow structures. All winglet deflections were observed to shift the right tip vortex core inboard, and thereby shorten the effective span of the wing. The effect of a winglet deflection may be approximated as a change in the wing aspect ratio and a lateral shift in the wing aerodynamic center. Prandtl's lifting line theory provides a closed-form estimate for the reduction in lift caused by a winglet deflection. A geometrical argument was made to account for the induced roll moment. The right tip vortex core also shifts vertically, following the deflected wing tip. Vertical shifts in the right tip vortex result in an angle between the wing span line and a line connecting the two tip vortices. A positive angle is defined as the right tip vortex higher over the wing than the left, and it is accompanied by a positive roll moment. While in sideslip, the wing with no winglet deflection experiences a considerable roll moment as a result of a vertical and lateral shift in the two tip vortices. The articulated winglets are observed to partially mitigate these effects when the upstream winglet is actuated, and thus show promise as a direct means of disturbance rejection.

Nomenclature

$\mathcal{R}$	=	aspect ratio b^2/S (b/c for rectangular wings)
b	=	wing span
b_{eff}	=	effective aerodynamic span (distance between tip vortices)
b_w	=	winglet span
b'	=	wing span with winglet deflected; $b - b_w(1-\cos(\delta_{\mathrm{Rt}}))$
C_L	=	lift coefficient; $L/(1/2)\rho U_\infty^2 S$
C_l	=	roll moment coefficient; $l/(1/2)\rho U_\infty^2 Sb$
C_{l_α}	=	coefficient of roll with respect to angle of attack ($\delta_{\mathrm{Rt}} \neq 0$ deg)
C_{l_β}	=	coefficient of roll with respect to sideslip
c	=	wing chord
e_ω	=	error in vorticity measurements
Re	=	Reynolds number $U_\infty c/\nu_\infty$
S	=	planform area
St	=	Strouhal number; fc/U_∞
U_∞	=	freestream velocity, ft/s
X, Y, Z	=	aerodynamic coordinates
x_b, y_b, z_b	=	body coordinates
α	=	angle of attack
α'	=	effective angle of attack (Prandtl)
β	=	sideslip angle, deg
Γ	=	circulation
ΔC_L	=	$C_L(\alpha,\beta,\delta_{\mathrm{Rt}}) - C_L(\alpha,\beta,0\ \mathrm{deg})$
ΔC_l	=	$C_l(\alpha,\beta,\delta_{\mathrm{Rt}}) - C_l(\alpha,\beta,0\ \mathrm{deg})$
$\Delta x, \Delta y, \Delta z$	=	particle image velocimetry grid spacing
δ_a	=	aileron deflection, deg
δ_{Rt}	=	right winglet deflection, deg
Θ	=	angle between tip vortices, deg
ν_∞	=	freestream dynamic viscosity, slug/(ft · s)
ρ_∞	=	freestream density, slug/ft^3
$\sigma_{u,v,w}$	=	standard deviation of velocity measurements

I. Introduction

Low-aspect-ratio wings exhibit low lateral aerodynamic damping and inertia [1,2]. These traits are exploited by fighter aircraft and other highly maneuverable air vehicles: both manufactured [3] and natural [4]. The penalty of this agility is that vehicles with low-aspect-ratio wings are often difficult to control when perturbed, particularly when those perturbations are lateral [5]. This leads to complications for the control of micro aerial vehicles (MAVs). MAVs commonly feature a low-aspect-ratio wing out of necessity to maximize lifting surface area with constraints on size [6–11]. As a result of flying at low Reynolds numbers in gusty environments [12], MAVs are often subject to large sideslip angles as well. In sideslip, the aerodynamic structures on the suction side of low-aspect-ratio wings [13,14] become asymmetric [15–17]. Figure 1 shows isovorticity contours from stereoscopic digital particle image velocimetry (S-DPIV) measurements by DeVoria and Mohseni [16] of the flow about an $\mathcal{R} = 1$ rectangular wing at three different sideslip angles. The dominant tip vortices are integral to the reattachment of the leading-edge separation region (LESR) via their downwash [16]. Comparing the images in Fig. 1 from left to right shows how a lateral shift of the tip vortices leads to asymmetry in the LESR. This asymmetry results in an imbalance in lift distribution, and ultimately the generation of a roll moment [16]. The existence of this roll moment is a significant aerodynamic phenomenon inherent to these wings because they have neither wing sweep nor dihedral. Etkin [18] pointed out that planar wings in negative sideslip experience an inherent positive roll moment described by the static stability derivative $-C_{l_\beta}$. This effect is clearly exacerbated in low-aspect-ratio wings, as seen in Fig. 1 and explained by DeVoria and Mohseni [16]. Our group has shown [19] that the lateral and longitudinal dynamics are cross coupled though the tip vorticies which are a function of lift (and the tip vortices sustain the lift

Presented as Paper 2017-1270 at the AIAA Guidance, Navigation, and Control Conference, AIAA SciTech Forum, Grapevine, TX, 9–13 January 2017; received 14 August 2017; revision received 13 April 2018; accepted for publication 1 November 2018; published online 28 January 2019.

*Graduate Research Assistant, Department of Mechanical and Aerospace Engineering. Student Member AIAA.

†William P. Bushnell Endowed Chair, Mechanical and Aerospace Engineering Department and Electrical and Computer Engineering Department. Associate Fellow AIAA.

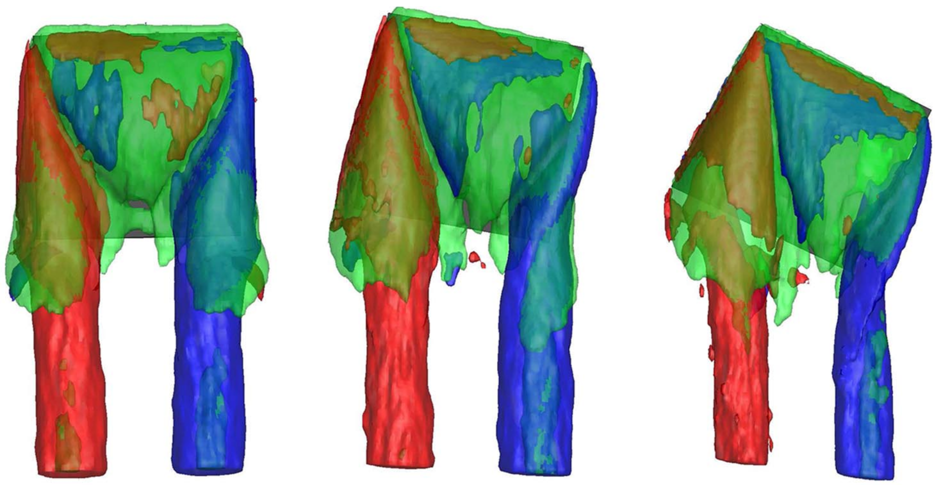

Fig. 1 S-DPIV measured isovorticity contours: cross-stream vorticity shown in green, positive streamwise vorticity shown in blue, and negative in red. $Re = 8 \times 10^4$, from DeVoria and Mohseni [16].

enhancing LESR). This implies the lateral response to sideslip perturbations is cross coupled with the angle of attack. Untapered low-aspect-ratio wings in sideslip exhibit an increase in the magnitude of $-C_{l_\beta}$ up to a large angle of attack where after the $-C_{l_\beta}$ derivative drops precipitously. This occurs before the wing experiences stall. The sharp inflection of the roll moment with a pre-tall change in angle of attack is termed "roll stall" [15]. While considering the wing dynamics, Shields and Mohseni [20] found that sideslip reduces pitch stability in low-aspect-ratio wings and the ensuing oscillations in the angle of attack will cause a coupled Dutch-roll-like mode to diverge as a result of the time-varying C_{l_β}. This divergent coupled mode is referred to as "roll resonance" [20]. The tip vortices themselves are formed by rollup of the shear layer at the tip of each wing. Therefore, control of the individual tip vortex formations gives the potential to mitigate a significant source of lateral moments on low-aspect-ratio wings. We propose using a pair of independently actuated winglets as roll control surfaces.

Discrete hinged surfaces are typically used on fixed-wing aircraft to generate aerodynamic forces for aerodynamic control. The lateral instability of low-aspect-ratio wings is mitigated by the addition of artificial roll and yaw damping via the actuation of these control surfaces under the guidance of a closed-loop controller, such as a human pilot or stability augmentation system. Traditionally, control flaps are located at the rear edge of each lifting surface and only affect the chordwise curvature of the wing or tail on which they are attached. Lateral control is then accomplished by varying the chordwise geometry (e.g., aileron flaps, differential tail flaps, spoiler flaps, and rudder deflections) of the wings or tails in a manner that is asymmetric about the airplanes plane of symmetry. Such control surfaces may be designed using a two-dimensional assumption about the change in sectional wing lift [21–23], such as the strip hypothesis [24]. Unfortunately, low-aspect-ratio wings confound many of the assumptions these theories are founded upon. This is due to the highly three-dimensional nature of the wing aerodynamics [6,16,17], as seen in Fig. 1, and because of the LESR, which represents bound circulation on the wing itself [19].

Low-aspect-ratio wings also have the ability to sustain lift to high angles of attack before stall. At high angles of attack, the rear edge flaps become enveloped by the leading-edge shear layer as the reattachment point of the LESR moves aft. Fischel et al. [25] observed a reduction in aileron effectiveness due to a decrease in both the aileron moment arm and the wing sectional lift independence on low-aspect-ratio wings. To compensate for this, an increase in the flaps wetted area or deflection angle is required, which results in further loss of flap efficiency [1]. Although conventional ailerons might not be an ideal control surface on low-aspect-ratio wings, traditional flap control surfaces are attractive because they typically consume little power to actuate. The choice of articulated winglets as lateral control surfaces marries the ideas of using simple flap control surfaces and placing them at a location of aerodynamic significance on low-aspect-ratio wings.

Winglets in their present form were first developed by Whitcomb [26] as symmetric attachments to the wing tips to increase wing efficiency. They behave essentially as a wing extension by providing a reduction in induced drag without the direct addition of span [26,27]. Although many commercial transport aircraft employ fixed cant angle winglets now, Whitcomb [26] noted that the winglet height or cant angle may be optimized for different lift coefficients. Varying the winglet cant angle during flight has been investigated [28,29] as a means to maximize wing efficiency through different phases of a vehicles flight. Perhaps one of the most dramatic examples of variable cant angle winglets for this purpose is the wing of the XB-70 Valkyrie: the wing tips of which would be planar during takeoff, and then cant downward more than 60 deg in flight to reduce drag during supercruise [30]. The use of variable cant angle winglets has also been explored for vehicles at the MAV scale. The use of jointed wings with passively hinged tips was found to increase the robustness of lateral stability [31] and damp longitudinal dynamic modes [32] on small-scale vehicles. Work by Broudin et al. [33,34] explored the concept of using actively articulated winglets for lateral control on a swept flying wing. Their work demonstrated that large winglets (widths 25 and 50% of span) are viable lateral control surfaces. For some turn radii, they found the winglets would even provide the proverse yaw moment necessary to conduct a coordinated turn. This is due to the inward lift generated by the upward deflected winglet of the interior wing. Because the wing under investigation in their work had positive sweep, the articulated winglet configuration provided a means of controlling the longitudinal stability margin. Winglet deflections therefore provided the control to induce a pitching moment or trim the flying wing about a desired angle of attack. This change in pitching moment was also observed by Whitcomb, but the effect was considered small enough to trim out [26].

The study presented in this paper explores the use of smaller winglets (width 9% span) on aspect-ratio-one wings without sweep. These winglets are placed along the full length of the tips of the wing and hinge in the chordwise direction, akin to the polyhedral created by the deflection of the tip feathers on a bird wing [35]. This study proposes a model for winglet control authority on low-aspect-ratio wings with zero sweep angle.

An overview of the wind-tunnel setup used for aerodynamic loading and S-DPIV measurements is given in the next section (Sec. II). To illustrate the effect the winglet control surfaces have on the tip vortices in the near wake, S-DPIV flow imaging is presented in Sec. III. The force measurement data are presented as nondimensional coefficients of lift and roll and explained in the Aerodynamic Loading Results section (Sec. IV). The aerodynamic forces of the wings in sideslip are presented, and the applicability of the articulated winglets to mitigate sideslip effects is commented on in Sec. IV.C. A closed-form model is proposed in Sec. V based on an analogy between winglet deflections and changes in wing aspect ratio. Finally, the work is summarized and conclusions about the applicability of articulated winglets as lateral control surfaces on low-aspect-ratio wings are presented in Sec. VI.

II. Experimental Setup

A. Wind-Tunnel Testing

Data in this study were collected by testing conducted in a closed-loop wind tunnel made by Engineering Laboratory Designs. The test section of this tunnel measures 4 ft long with a 2 ft^2 cross section. The tunnel is capable of producing a top flow velocity of 280 ft/s; although for this work, a tunnel speed of 32.52 ft/s was set to achieve the desired chord-based Reynolds number Re of 100,000. After conditioning, the flow enters the acrylic-walled test section with a freestream turbulence intensity of 0.12%

B. Wings Tested

Two flat-plate (0% camber) wings were tested in this study: one with conventional rear-mounted aileron flaps and one with hinged wing tips. Both wings are square with an aspect ratio of one, have a chord length of 0.5 ft, and are made of acrylic. The wings have a thickness-to-chord ratio of 1.6%, and the leading edges of the wings are beveled with a 5 : 1 symmetric elliptical profile. Diagrams of both wings with the body coordinate system and control surface deflection definitions are shown in Fig. 2. The body coordinate system [1,2,36] has its origin at the quarter-chord point, and the spanwise centerline on the wing and aerodynamic angles are labeled with respect to it. The aileron deflection angle, seen in Fig. 2a, describes an equal and opposite deflection of the right and left flaps in the canonical way [1]. The aileron flaps measure 0.15c chordwise by 0.25c spanwise. The aileron flaps extend just short of the wing center to accommodate the attachment point of the force balance. The independent articulation of the two winglet control surfaces must be described by two angles: one for each surface. In this study, right-hand-positive rotations about the right winglet hinge are considered positive: that is, right wing tip-down deflections are positive right winglet deflections. This convention was adopted by obeying the standard method of describing control surface deflections [1]. The diagram in the bottom of Fig. 2b illustrates the full set of deflections at which data were collected. In this study, deflections of the right winglet were adjusted while the left winglet was held planar with the wing. The articulated winglets are the full length of the chord deep and measure 0.09c spanwise. In an attempt to compare the dissimilar control surfaces, the wetted surface area of the ailerons are identical to the winglets.

Aerodynamic loading data are presented, acting at the origin of the body coordinate system. However, it was more illustrative to present the S-DPIV flow imaging results with respect to an alternate aerodynamic or "laboratory" coordinate system. The laboratory reference frame is orthogonal with the freestream and has its origin defined by being aligned with the geometric center of the wing models. The laboratory and body reference frames are shown together in Fig. 3.

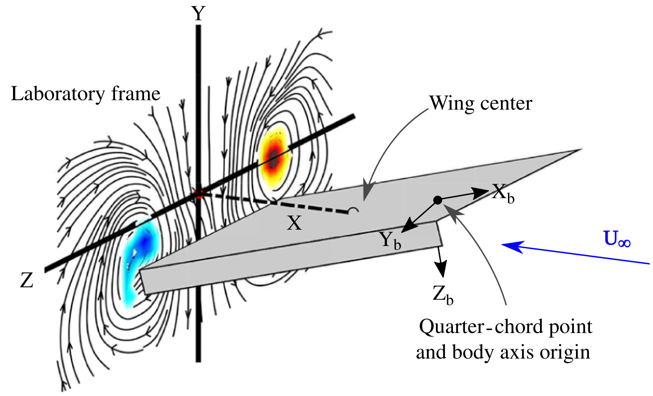

Fig. 3 S-DPIV cross-stream velocity and streamwise vorticity (blue positive) data shown with both laboratory and body axes labeled. Right winglet is deflected $\delta_{Rt} = 90$ deg.

C. Aerodynamic Loading Measurement

A custom robotic model positioning system (MPS) was built in house to facilitate automated positioning of models in the wind tunnel. A diagram of the MPS is shown in Fig. 4a. The MPS is actuated by four electric stepper motors controlled by LabVIEW hardware and software. This configuration allows roll, pitch, and yaw angles to be set independently of each other. Through programmed profiles, the MPS may also execute dynamic single- and multiaxis maneuvers, although these were not required for the present study. The MPS was developed to hold models from the rear and presents a slim profile to the oncoming flow as shown in Figs. 4b and 4c. For the present study, the wings' bank angle was held at zero and the tunnel freestream was aligned with the laboratory X axis. This allowed the angle of attack to be set by varying the MPS pitch angle, as shown in Fig. 4c; and it allowed sideslip to be created by varying the yaw angle, shown in Fig. 4b. In this configuration, the sideslip angle is the negative of the yaw angle.

The aerodynamic loadings of the test wings were measured with a six-degree-of-freedom force balance sting manufactured by Micro Loading Technology. The force balance was custom made to measure the aerodynamic load magnitudes of full-scale MAV and MAV scale models. The degrees of freedom recorded are normal, axial, and side forces, as well as roll, pitch, and yaw moments. More details about the full force balance specifications can be found in Ref. [37].

Static loading was measured by holding each wing and control surface configuration at a set of aerodynamic angles for 10 s; the first 8 s were dedicated to allow the flow to reach steady state, and then measurements were taken for 2 s. The six channels of the force

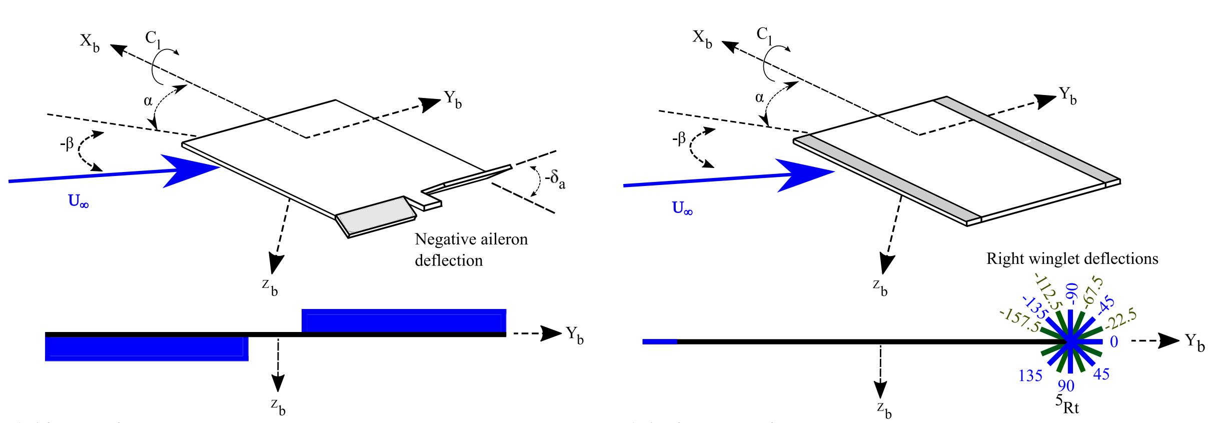

a) Aileron diagram **b) Articulated winglet**

Fig. 2 Schematic of 6 in. flat-plate test wings with body coordinate system, with control surfaces shaded.

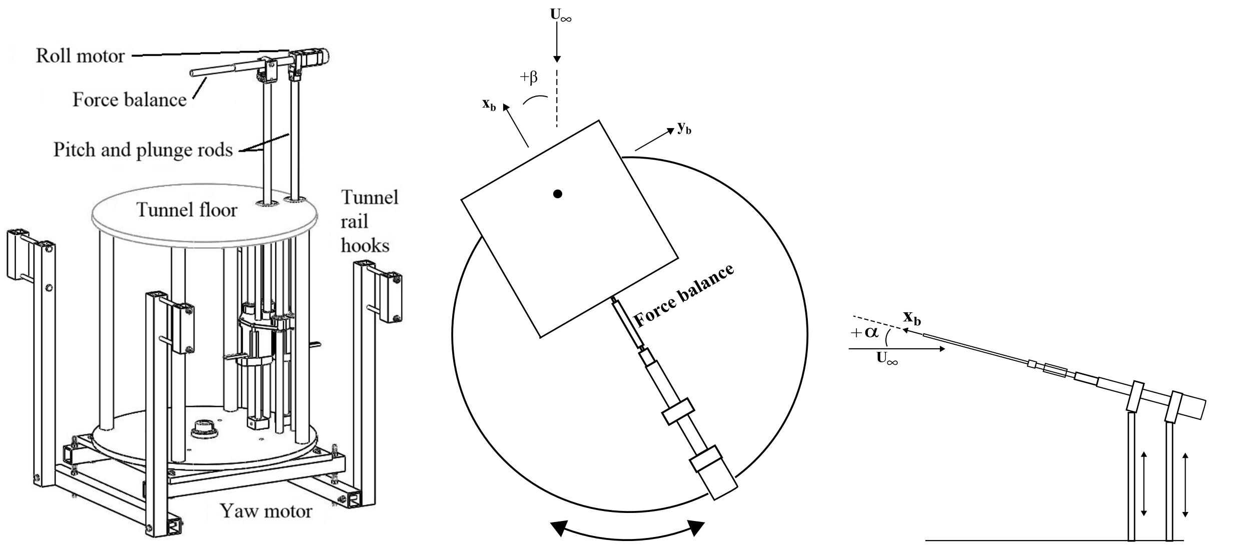

a) Model positioning system out of tunnel b) Top view of wing in positive sideslip c) Side view of wing at positive angle of attack

Fig. 4 Model positioning system diagrams.

balance were sampled at 2048 Hz to make a single data record of the average of 4096 voltage samples. The voltage samples were recorded by a National Instruments SCXI-1520 eight-channel strain gauge module. The measurement record was processed through a low-pass Butterworth filter set at 1 kHz to remove aliasing; the analog voltage signals were then converted to digital streams by a 16-bit A/D converter. The digital voltage measurements were converted into physical loads using the AIAA standard iterative method for strain gauge measurements [38].

Calibration of the force balance test setup was performed before each test series. This includes an extended warmup period for the system to reach thermal equilibrium, followed by calibration using known masses. To simultaneously validate the positioning accuracy of the MPS, the wind-tunnel settings, the inertial taring procedure, the force balance readings, and data postprocessing a model dataset of an $\mathcal{R} = 1$ flat plate were collected and compared to the data from previous studies in Refs. [7,37] (both of which were from different model holding systems and tunnels). Force measurements by this study's test setup were found to agree with Refs. [7,37] to within 0.05% of the full-scale force readings. This level of accuracy produces error bars within the figure markers for the plots in this paper. All force data presented have been nondimensionalized by the dynamic pressure and wing planform area. The longitudinal pitching moment is nondimensionalized using the chord length as the reference length scale, whereas the lateral moments of roll and yaw are nondimensionalized using the wing span. For consistency, the planform area, chord length, and span length are those of the wings without control surface deflections.

D. Stereoscopic Digital Particle Image Velocimetry Measurements

A high-speed S-DPIV setup was used to capture two-dimensional three-component measurements of flow velocity directly behind the trailing edge of the model and orthogonal to the freestream. Stereoscopic images were captured using two high-speed Phantom cameras ($v210/v210$, 1280×800 pixels^2). The image plane was illuminated by a Quantronix Darwin-Duo 20 mJ Neodymium-doped yttrium lithium fluoride ($\gamma = 527$ mm) high-speed laser capable of a 10 kHz firing frequency. All laser pulses and exposures were synchronized by a Laserpulse 610036 timing unit. S-DPIV processing and stereoscopic reconstruction were performed by TSI Insight 4G software using an object-to-image mapping [39] function calibrated by images of a precision-machined dual-plane target. Slight misalignment of the target with the laser sheet were corrected by a disparity map [39–41] created from 1000 image pairs of the freestream. The interframe time for S-DPIV capture was selected to balance the particle residency time while maximizing dynamic range [41]. Selecting the interframe time is critical because imaging was conducted with the freestream component of flow coming through the 1.6-mm-thick laser plane. The particle residence time is proportional to the signal-to-noise ratio, whereas the dynamic range is proportional to the length of the interframe time. The image pairs from each camera were processed into velocity vectors using Insight 4G software and a multipass interrogation window method with course grid size of 64×64 pixels^2, and then a fine grid size of 32×32 pixels^2 with 50% overlap. This resulted in chord-based vector spacing of $\Delta y = \Delta z = 0.0373c$. The total measurement plane was roughly $1c \times 2c$. The S-DPIV system was calibrated by measuring the empty tunnel flow using the same settings as were used for wake flow imaging. The statistics of the resulting 1000 realizations of freestream velocity field show in-plane velocity errors to be below 5% of the freestream velocity. The freestream test results are a worst-case scenario for the S-DPIV setup. The calibration test indicates the largest expected errors during wing testing due to the minute in-plane velocities and maximum through-plane velocity component. The two tip vortices are of primary interest in this study. It was found that the through-plane component of velocity in each vortex core was between 85 and 50% of the freestream value, and both tip vortex cores were found to have large cross-stream velocities. Both of these factors will reduce the error in the measurements presented in this study. Figure 3 shows the significant cross-stream velocity and vorticity fields with respect to a wing diagram.

The velocity field of each snapshot was analyzed to calculate an individual realization of the vorticity field, the turbulent kinetic energy (TKE) field, and a scalar field of the γ_1 criterion by Graftieaux et al. [42]. Computation of the fields from each snapshot allows the inspection of the time evolution and statistics for each field quantity to be calculated. Mean values of each field were computed from the ensemble average of the set of field snapshots. The vorticity was computed using the local circulation method [41], which is an integral method and reduces random measurement errors that may be present in the velocity field. The error in vorticity as a result of errors in the velocity field is $e_\omega = 1.38\sigma_v/\Delta x$, and it is below the cutoff threshold for identifying tip vortex vorticity. The TKE field was computed by taking the root-mean-square sum of the fluctuation components of the in-plane velocity components. The tip vortex core locations were identified using the γ_1 criterion by Graftieaux et al. [42], in which the orthogonality of the vector field about a point is measured. This method reliably found the center of each tip vortex as would be recognized by a human observer or in qualitative smoke visualization. The time-averaged tip vortex locations are found from the Euclidean mean of instantaneous core locations at each snapshot. Computation of each snapshot's field values facilitates a time-resolved analysis as well as commentary of the movement of the tip

Table 1 Test matrix of data collected

Parameter	Value
	Force data
Wing orientations	$\alpha = [0\ \text{deg}, 2\ \text{deg}, \ldots, 46\ \text{deg}]$, $\beta = [-20, -10, 0, 10, 20]$ deg
Control surface deflections	$\delta_a = [-10, -20, -30, -45, -55]$ deg
	$\delta_{\mathrm{Rt}} = \pm[0, 22.5, 45, 67.5, 90, 112.5, 135, 157.5, 180]$ deg
	S-DPIV data
Wing orientations	$\alpha = 15$ deg, $\beta = [-20, -10, 0, 10, 20]$ deg
Control surface deflections	$\delta_a = [-45]$ deg $\delta_{\mathrm{Rt}} = \pm[0, 45, 90, 135]$ deg

vortices. Due to the low-velocity errors, the random nature of particle image velocimetry velocity (PIV) errors, and the use of integration methods to calculate field quantities, the limiting source of uncertainty in the estimation of the tip vortex locations is the PIV vector grid spacing. The effects of the grid resolution are presented as error bars in the tip vortex core location plots presented in the Results section (Sec. IV).

E. Test Matrix

Aerodynamic loading data were measured with the wings held at five sideslip angles of $\beta = [-20, -10, 0, 10, 20]$ and a range of angles of attack of $\alpha = [0\ \text{deg}, 2\ \text{deg}, \ldots, 46\ \text{deg}]$. This distribution of aerodynamic angles was chosen because the predominant parameter affecting wing aerodynamics is the angle of attack. Datasets with a high resolution of sideslip angle at fixed angles of attack were also collected for thoroughness. These results are not presented here because the five sideslip angles measured are sufficient to describe the observed trends. Sixteen different right winglet deflections and six aileron deflections were measured at every pair of aerodynamic angles. Right winglet and negative aileron deflections were measured, leveraging the symmetry of the wings; this constitutes a full set of aileron and independent winglet deflections. The testing matrix of the force measurements presented in this study is described in the upper half of Table 1. All S-DPIV testing was conducted with the wing models at $\alpha = 15$ deg. This angle of attack was chosen due to observations of the aerodynamic loading data, which indicate $\alpha = 15$ deg is the maximum angle at which winglet control authority grows linearly with angle of attack. The wing configurations measured with the S-DPIV setup are enumerated in the lower half of Table 1.

III. Wake Flow Imaging

The wake flow imaging results presented in Figs. 5 and 6 explain how the tip vortex locations are a function of sideslip and right winglet deflection angles. All imaging was conducted at one angle of attack: $\alpha = 15$ deg. This angle of attack was selected because it is the maximum angle of attack at which winglet control authority increases linearly with lift. Figure 5 shows all time-averaged flowfields measured in this study and depicts trends in flow topology as a function of sideslip and winglet deflection angles. (Note that, in Fig. 5, the cross-stream velocity field is shown as vectors, the positive streamwise vorticity is shown in red, the negative streamwise vorticity is shown in blue, black ellipses outline instantaneous tip vortex core locations, and gray contour lines depict the TKE field.) The origin of each plot is the laboratory reference frame, which was previously shown in a diagram in Fig. 3. The center plot of Fig. 5 shows the wing at zero sideslip and without winglet deflection ($\beta = \delta_{\mathrm{Rt}} = 0$ deg) and serves as a comparison for all other plots. The field quantities shown in each panel of Fig. 5 are depicted as follows.

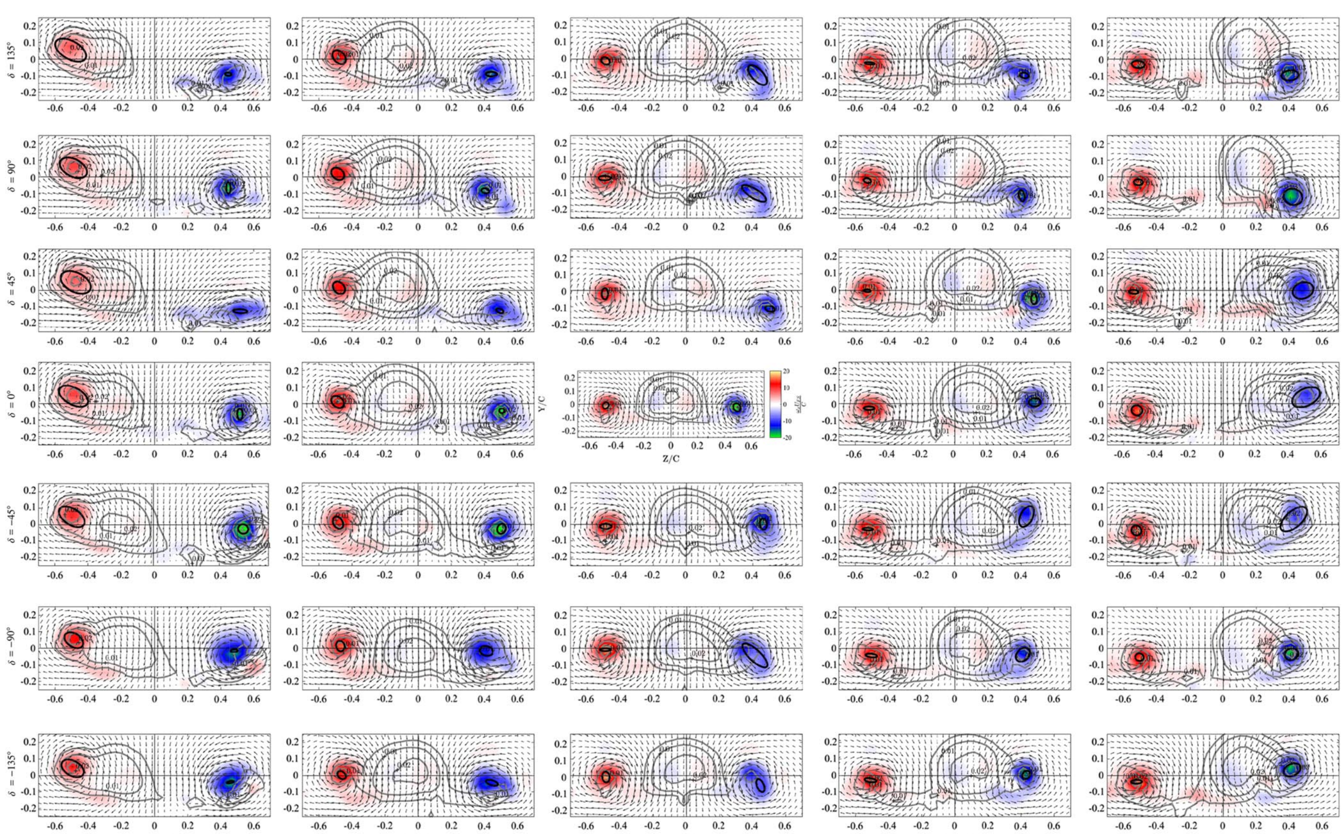

Fig. 5 S-DPIV imaging of near-field wake flow behind $\mathcal{R} = 1$ models with right tip deflections δ_{Rt} and sideslip perturbations β at $\alpha = 15$ deg.

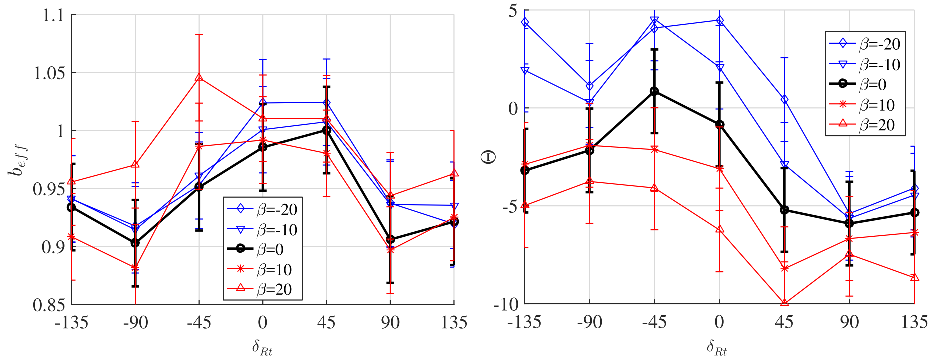

a) Changes in distance between cores vs δ_{Rt} **b) Angle between cores vs δ_{Rt}**

Fig. 6 The distance between tip vortices b_{eff} (Fig. 6a), and the angle formed by the two tip vortices with respect to the horizontal axis Θ (Fig. 6b). Aspect-ratio-one wings held at $\alpha = 15$ deg and varied in sideslip β.

The cross-stream velocities U_Y and U_Z are depicted as a vector field. The turbulent kinetic energy is depicted as a set of gray contour lines. The mean vorticity is shown as flooded contours, with red for positive and blue for negative vorticities. The distribution of time-resolved tip vortex core locations are shown as a black ellipse generated by the 2-norm of instantaneous tip vortex core locations. The cross-stream velocity field is depicted as a vector field to give a sense of the direction, relative magnitude, and symmetry of the tip vortex induced downwash near the trailing edge of the wing. The wake flow behind the low-aspect-ratio wings tested departs from slender wing theory in that their trailing wake is highly nonplanar even in the near wake. Imaging of the near-field wake flow bisects both trailing tip vortices and the turbulent flow being shed from the aft section of the LESR.

The goal of the imaging was to measure the effect of winglet deflection on the suction-side flow structures. Changes in the lateral symmetry of the near wake present an indication of lateral moments and forces on the wing. The downwash field appears to have its symmetry halfway between the two tip vortices and orthogonal to a line connecting the right and left core locations. This concept is important because the right winglet is observed to shift the right tip vortex along both the Y and Z directions, and thereby change the downwash field. In all cases, the strongest crossflow is seen over the top side of the wing tip vortices as the tip vortices impart momentum. The mean vorticity in the near wake is shown to be concentrated in the two tip vortices. Circulation was observed to vary only slightly between the two tip vortices in the near wake.

The wake deficit and peak TKE field centroid are seen to be a strong function of sideslip, shifting toward the downstream wing tip. Remembering Fig. 1 in the Introduction (Sec. I), which shows a three-dimensional view of the two tip vortices and the LESR, and comparing it with the center five plots in Fig. 5, we see the TKE field centroid coincides with the centroid of the wake velocity deficit region aft of the LESR. Globally, the LESR shifts laterally with sideslip ($+Z$ with $+\beta$), whereas the tip vortices maintain their lateral station and move vertically. In positive sideslip, the downstream tip vortex moves vertically upward ($+Y$), whereas the upstream tip vortex moves downward ($-Y$). It is shown later that winglet deflections affect a similar vertical shift in the tip vortex trailing the winglet.

A. Tip Vortex Locations

If we consider the location of the right and left tip vortices together, we may report their distance apart and the angle formed between them. Figure 6a shows the distance between the right and left tip vortex cores projected on the Z axis, whereas Fig. 6b shows the angle a line between the cores forms with the Z axis. Θ is positive when the right tip vortex core is further from the wing than the left. Both figures may be interpreted as changes in the location of the right tip vortex core because the location of the left vortex core was observed to be invariant under right winglet deflections. Figure 6a shows the right vortex core location is moved inboard proportional to $\cos(\delta_{\mathrm{Rt}})$. Figure 6b shows that vertical displacement of the right tip vortex follows the right wing tip: upward for -90 deg $\leq \delta_{\mathrm{Rt}} < 0$ deg forming a positive Θ angle, and downward for 90 deg $\geq \delta_{\mathrm{Rt}} > 0$ deg forming a negative Θ angle. The distance between the vortex cores (Fig. 6a) is shortened by all right winglet deflections. Work by Kaplan et al. [43] showed that, for low aspect wings, the distance between the tip vortices projected orthogonal to the wind Z axis can be considered as the effective aerodynamic span b_{eff}. The aerodynamic span is directly proportional to lift though the Kutta–Joukowski theorem by $L = \rho U_\infty \Gamma b_{\mathrm{eff}}$. The circulation of the tip vortices was observed to change only slightly as a function of sideslip while $\delta_{\mathrm{Rt}} \neq 0$ deg, and it is considered a negligible indicator of asymmetry. With the freestream velocity and flow density also constant, the only parameter left to affect lift is b_{eff}. It will be shown in the following section that lift is indeed reduced with b_{eff} and is symmetric about $\delta_{\mathrm{Rt}} = 0$ deg. The antisymmetric trend shown in Fig. 6b is interesting because it depicts a twist of the tip vortex pair with respect to the wing as a function of δ_{Rt}. This twist angle is also seen in the tip vortex system when $\delta_{\mathrm{Rt}} = 0$ deg and $\beta \neq 0$ deg, where positive Θ it is accompanied by a positive roll moment. In the following section that explains the aerodynamic loading data, it will be shown that both the symmetric lateral movement and antisymmetric vertical movement of the right tip vortex result in roll moments.

B. Unsteady Aerodynamics

The steady representation of the near-wake velocity field is a useful approximation as a comparison to the mean aerodynamic loading data; yet, some unsteadiness is observed in the wake flow imaging. Most notably, the tip vortices are seen to wander. The 2-norm of snapshot vortex core locations is shown in Fig. 5 as the black ellipses, which are sized to contain 95% of all instantaneous core location realizations. Inspection of the tip vortex core location ellipses shows that, where the tip vortex wanders, it generally does so with a preferred axis of travel. The tip vortex is observed to wander most when it is behind the downstream wing edge in sideslip or the behind the wing tip with a large winglet deflection. The ellipse of wandering tip vortex core locations generally forms an angle with the aerodynamic Y axis. The travel of the left and right tip vortex cores along the major axis of their respective elliptical distributions is correlated in time. When the left core is outboard, the right core is inboard toward the center span. This indicates the global suction-side vortex system comprising the LESR and tip vortices behaves as a coupled dynamic system. The two tip vortices oscillate in this manner at a frequency of approximately 55 Hz, or a Strouhal number using the chord and freestream of $St = 0.85$. The preferred direction of core wandering is seen to be an inclination of 45 deg to the horizontal. This is suggestive of the short-period mode instability seen by Leweke and Williamson [44]. The alternating correlated movement and angled direction of travel are conducive to developing the symmetric mode Crowe instability [45] in the far field. Sideslip is seen to generate the largest-amplitude core wandering in the downstream tip vortex; this comes as no surprise because the downstream wing edge is not directly energized by the freestream. Rather, the downstream tip vortex contains the leading-edge shear layer after it passes over the LESR. Winglet deflections cause the core of the tip vortex downstream of the winglet to wander. The tip vortex core wandering pattern is more erratic than the wandering pattern seen behind the downstream wing tip of the wing in sideslip. This is evinced by the lower eccentricity of the tip vortices' wander ellipses than those induced by sideslip. Preliminary data taken by the authors show the wander frequency to be a function of angle of attack. An $\mathcal{R} = 1$ wing inclined at $\alpha = 35$ deg exhibited larger-amplitude oscillations of the same nature at a much slower frequency of 9 Hz, $St = 0.14$.

IV. Aerodynamic Loading Results

A. Wing Lift Response

The coefficient of lift as a function of angle of attack at zero sideslip and for the full set of right tip winglet deflections and aileron deflections are shown in Fig. 7. All winglet deflections (tip down shown in Fig. 7a, and tip up shown in Fig 7b) are observed to reduce C_{L_α}, with the most extreme deflections increasing the angle of attack where stall occurs. This behavior is similar to (and, in the case of $\delta_{\mathrm{Rt}} = 180$ deg, identical to) the effect that the reducing aspect ratio has on C_L and C_{L_α}. Figure 7c shows that canonical rear-mounted aileron flaps do not change C_{L_α} but instead cause disruptions to the trailing edge, which result in earlier liftoff of the LESR and stall at shallower angles of attack.

Isolating the changes in lift induced by deflecting the right tip winglet, we plot the quantity ΔC_L versus δ_{Rt} in Fig. 8, in which

$$\Delta C_L = C_L(\alpha, \beta, \delta_{\mathrm{Rt}}) - C_L(\alpha, \beta, \delta_{\mathrm{Rt}} = 0 \text{ deg})$$

is the change in lift as a result of the winglet deflection. Figure 8b shows the changes in lift induced by the winglet deflection to be nearly symmetric about $\delta_{\mathrm{Rt}} = 0$ deg. When the wing is not in sideslip, all winglet deflections result in a decrease in lift. This concept may seem counterintuitive because winglets are considered lift-increasing devices. For the wings tested, the lift enhancement given by winglets is less than that of a wing tip extension of the same length when the wing is not in sideslip. When the data in Fig. 8a are scaled by $C_L(\alpha, \beta, \delta_{\mathrm{Rt}} = 0 \text{ deg})$, there is a general collapse of the data to the trend of $\alpha = 20$ deg. Although the wing is not in sideslip, changes in the right winglet deflection have a self similar effect on lift at different angles of attack. However, this is not the case for when the wing is in sideslip. The data in Figs. 8a and 8c, in which $\beta \neq 0$ deg, do not collapse when scaled by $C_L(\alpha, \beta, \delta_{\mathrm{Rt}} = 0 \text{ deg})$. This indicates the sign of winglet deflection is also of importance when the wing is in sideslip. A comparison of lift in negative sideslip shown in Fig. 8a, with lift in positive sideslip shown in Fig. 8c illustrating that sideslip has a similar and opposite effect on the trends of lift with winglet deflection. Although lift is still generally decreased symmetrically about $\delta_{\mathrm{Rt}} = 0$ deg, there exists an antisymmetric trend superimposed by sideslip. Lift is slightly increased for shallow negative winglet deflections while in negative sideslip, as well as for slightly positive winglet deflections while the wing is in positive sideslip. This effect on lift is ubiquitous across all angles of attack while the wing is in negative sideslip; and it is ubiquitous across all angles of attack only for large angles of attack while in positive sideslip, in which the deflected winglet is on the upstream wing edge. It is plain to see that the winglet deflection sign and whether the winglet is located on the right or left wing edge are of little importance to lift while the wing is not in sideslip. When the wing is in sideslip the downstream winglet deflection is of most importance.

B. Wing Roll Moment Response

Although deflections of the winglet change the wings' global lift, the control surface itself is located asymmetrically on the right wing tip and affects the distribution of lift asymmetrically as well. The asymmetry of lift on the wing imparts a torque about the geometric center of the wing. This is measured as a roll moment. The roll

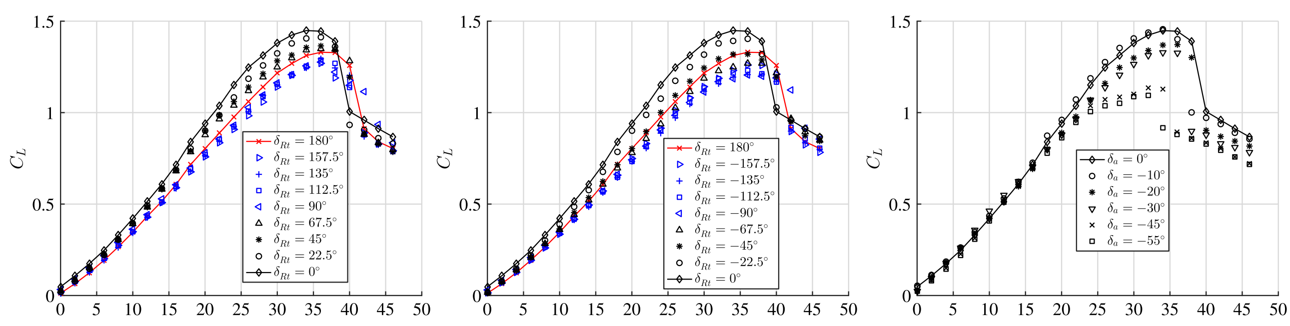

a) $\beta = 0$, $\delta_{Rt} \geq 0°$ (tip down) b) $\beta = 0$, $\delta_{Rt} \leq 0°$ (tip up) c) $\beta = 0$, $\delta_a \leq 0°$

Fig. 7 Lift as a function of angle of attack ($\beta = 0$ deg) at positive (wing tip down) and negative (wing tip up) winglet deflections δ_{Rt} and negative (right wing flap down) aileron deflections δ_a. Data were collected at $Re = 1 \times 10^5$ of an aspect-ratio-one wing.

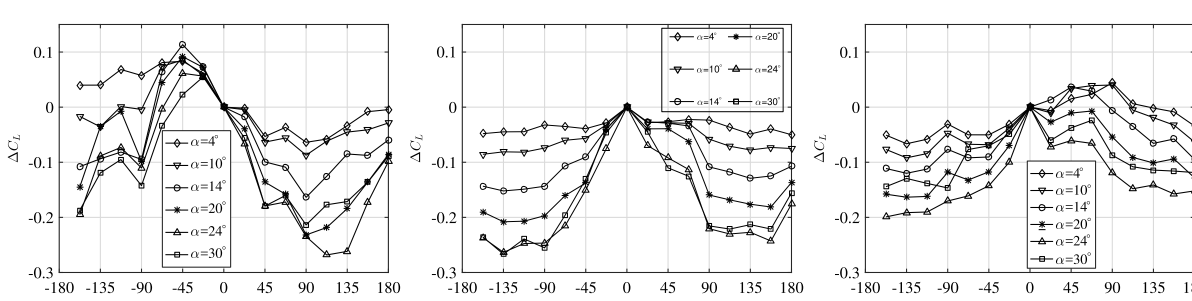

a) $\beta = -20°$ b) $\beta = 0°$ c) $\beta = 20°$

Fig. 8 Changes in lift $\Delta C_L = C_L(\alpha, \beta, \delta_{\mathrm{Rt}}) - C_L(\alpha, \beta, \delta_{\mathrm{Rt}} = 0 \text{ deg})$ as a function of winglet deflection angle δ_{Rt} at different angles of attack and three sideslip angles on an aspect-ratio-one wing.

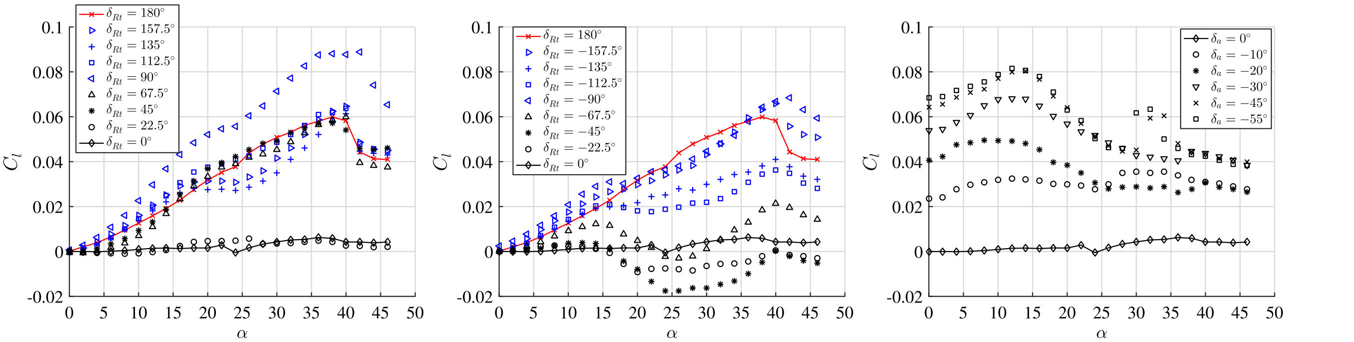

a) $\beta = 0$, $\delta_{Rt} \geq 0°$ **(tip down)** **b)** $\beta = 0$, $\delta_{Rt} \leq 0°$ **(tip up)** **c)** $\beta = 0$, $\delta_a \leq 0°$

Fig. 9 Roll moment as a function of angle of attack ($\beta = 0$ deg) at positive (wing tip down) and negative (wing tip up) winglet deflections δ_{Rt} and negative (right wing flap down) aileron deflections δ_a.

moment generated by deflections of the right articulated winglet while holding the left tip neutral is plotted as a function of angle of attack in Fig. 9. Figure 9a shows the roll moment response of the winglet tip down $+\delta_{\mathrm{Rt}}$, Fig. 9b shows the roll moment generated by winglet tip-up $-\delta_{\mathrm{Rt}}$ deflections, and Fig. 9c shows negative aileron deflections $-\delta_a$. Inspection of Figs. 9a and 9b shows that the positive roll moment linearly increases with angle of attack for all tip-down $\delta_{\mathrm{Rt}} > 0$ deg deflections and large tip-up $\delta_{\mathrm{Rt}} < -90$ deg deflections. This trend begins at zero for all δ_{Rt} and increases up to $\alpha = 15$ deg. This indicates the primary generator of roll moment is directly linked to global lift as the roll moment increases with lift until stall. The subset of winglet deflections 0 deg $< \delta_{\mathrm{Rt}} < -90$ deg generates a small roll moment up to high angles of attack ($\alpha > 15$ deg) in which the only reverse ($C_l < 0$) roll moments are observed. In this subset of deflections, the shallow tip-up deflections are streamlined to the oncoming flow, particularly at high angles of attack. These shallow tip-up winglet deflections are observed to shift the right tip vortex upward and reduce the twist angle Θ between the tip vortices and wing as shown previously in Fig. 6b. In shallow tip-up deflections, the height of the right wing tip vortex above the wing is increased and nullifies, or even reverses, the roll moment generated by the asymmetric decrease in lift (see Fig. 8b). Aside from this subset of δ_{Rt}, all other deflections generate a nearly linearly increasing roll moment with an increase in α. The maximum roll moment is generated by $\delta_{\mathrm{Rt}} = 90$ deg, where massive disruption is induced to the side edge flow. For winglet deflections other than shallow tip-up ones, the roll moment authority achieved limits to a fully folded winglet deflection of $\delta_{\mathrm{Rt}} = 180$ deg, shown as a red line in Figs. 9a and 9b. For all tests, both winglet and aileron, there is a notable departure from linearity at $\alpha = 15$ deg, meaning that the slope, or $C_{l_\alpha}(\delta_{\mathrm{Rt}} \neq 0$ deg), of each plot changes. This is attributed to a change in the suction-side flow structures as the LESR becomes established [16].

A model wing with rear-mounted aileron flaps of the same wetted surface area as the articulated winglets was tested. The results shown in Fig. 9c are provided to compare the articulated winglet roll control authority to a canonical control surface. The aileron control surfaces affects a differential camber of the wing. This camber is present even when $\alpha = 0$ deg, and thus we observe a roll moment at a zero angle of attack. The conventional aileron control authority seen in Fig. 9c also attenuates at high angles of attack, unlike the roll moments generated by deflected winglets. Authority is seen to increase slightly up to $\alpha = 15$ deg when the LESR begins to grow and the low-aspect-ratio flow structures deviate from canonical high-aspect-ratio wings. The roll moment is seen to attenuate like a stall at larger angles of attack well before general wing stall. This is an effect of localized stall as a result of large local camber. Local stall results in global disruption to the LESR and tip vortex system of flow structures.

Generally, control surfaces affect a monotonic aerodynamic moment or force with respect to deflection angle. This linearity allows a single scalar value of the relationship between deflection and roll moment such as, ($C_{l_{\delta_{\mathrm{Rt}}}} = (\partial C_l / \partial \delta_{\mathrm{Rt}})$), to describe the control authority. The roll moments generated by articulated winglet deflections, however, are not globally monotonic. Figure 10 shows the control authority of the articulated winglet

$$\Delta C_l = C_l(\alpha, \beta, \delta_{\mathrm{Rt}}) - C_l(\alpha, \beta, \delta_{\mathrm{Rt}} = 0 \text{ deg})$$

as a function of winglet deflection δ_{Rt} at six different prestall angles of attack and at three sideslip angles. Four distinct regions of deflection angles produce four different behaviors in roll moment. The regions are as follows: winglet deflections of -180 deg $< \delta_{\mathrm{Rt}} \leq -90$ deg, in which the winglet is folded over the wing; winglet deflections of -90 deg $< \delta_{\mathrm{Rt}} < 0$ deg, which are shallow tip-up deflections; winglet deflections of 0 deg $< \delta_{\mathrm{Rt}} \leq 90$ deg, which are shallow tip-down deflections; and winglet deflections of 90 deg $< \delta_{\mathrm{Rt}} \leq 180$ deg, in which the winglet is folded under the wing. Consider the case without sideslip shown in Fig. 10b first. Increases in shallow right winglet deflection ($|\delta_{\mathrm{Rt}}| \leq 90$ deg) result in an increase in roll moment. The relationship between the deflection and roll moment then saturate with deflections past $|\delta_{\mathrm{Rt}}| \geq 90$ deg. The change in roll moment with winglet deflection is globally symmetric about $\delta_{\mathrm{Rt}} = 0$ deg. This behavior is expected if the right wing tip is shortened by the projection

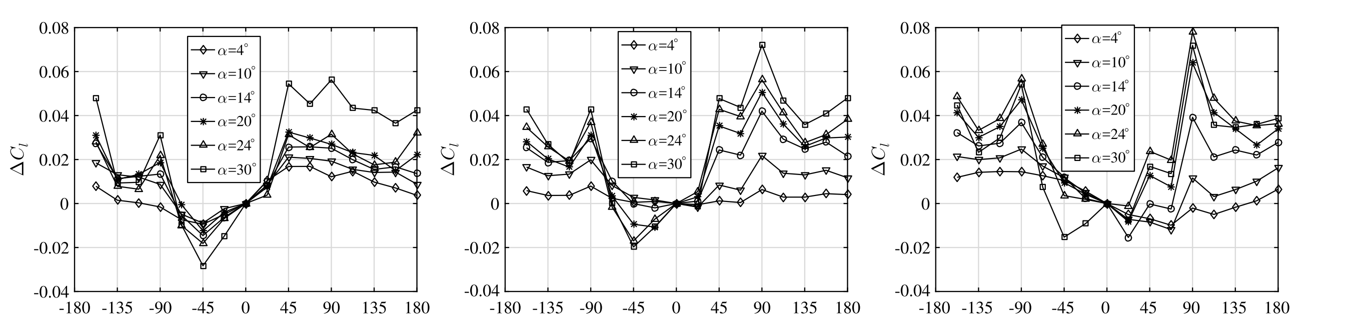

a) $\beta = -20°$ **b)** $\beta = 0°$ **c)** $\beta = 20°$

Fig. 10 Roll control authority $\Delta C_l = C_l(\alpha, \beta, \delta_{\mathrm{Rt}}) - C_l(\alpha, \beta, \delta_{\mathrm{Rt}} = 0$ deg) as a function of winglet deflection angle δ_{Rt} at different angles of attack and three sideslip angles.

of the winglet deflection $\cos(\delta_{\mathrm{Rt}})$. At large angles of attack, the sign of the winglet deflection becomes important as well. The trends in Fig. 10b for $\alpha > 14$ deg show that shallow tip-down deflections (0 deg $< \delta_{\mathrm{Rt}} < 90$ deg) actually generate a negative roll moment that increases in magnitude with positive δ_{Rt}. Although all winglet deflections result in a loss of lift that is nearly symmetric about $\delta_{\mathrm{Rt}} = 0$ deg for a wing at zero sideslip, only one deflection region (-90 deg $< \delta_{\mathrm{Rt}} < 0$ deg) generates a negligible or negative roll moment. This implies that, although the lift is reduced by the effective change in span as $|\delta_{\mathrm{Rt}}| > 0$ deg, deflections of -90 deg $< \delta_{\mathrm{Rt}} < 0$ deg do so in such as way that either no torque or negative torque is imparted on the wing from lateral asymmetry of the flow structures.

C. Wings in Sideslip

Sideslip is the predominant generator of roll moments on low-aspect-ratio wings due to the asymmetries of the suction-side flow structures it generates. Low-aspect-ratio wings without dihedral or any vertical surfaces generate significant adverse roll moments ($-\beta$ results in $+C_l$) in the presence of sideslip due to asymmetries in the tip vortices and LESR structure. With sideslip present, the roll moment effect is seen to increase as a function of angle of attack up to an event at which the roll moment drops in magnitude yet global lift stall has not occurred. This phenomena has been called roll stall [20], and it has the potential to destabilize low-aspect-ratio wings. By manipulating the tip vortices, articulated winglets are intended to directly control the source of roll moment generation: that is, the lateral asymmetry of the LESR.

Although Figs. 7 and 9 may be recreated for all four $\beta \neq 0$ deg sideslip values, it is more succinct to investigate the effect δ_{Rt} has on the lateral stability derivative C_{l_β}. Figures 11a–11d show this for each of the four deflection angle regions: folded tip up -180 deg $< \delta_{\mathrm{Rt}} \leq -90$ deg in Fig. 11a, shallow tip up -90 deg $< \delta_{\mathrm{Rt}} \leq 0$ deg in Fig. 11b, shallow tip down 0 deg $\leq \delta_{\mathrm{Rt}} < 90$ deg in Fig. 11c, and folded tip-down deflections 90 deg $< \delta_{\mathrm{Rt}} \leq 180$ deg in Fig. 11d. Aileron deflections are shown in Fig. 11e for reference. The most prominent feature of Fig. 11 is the linear decrease of C_{l_β} with increasing α up to roll stall around $\alpha = 20$ deg. The winglet defections of $|\delta_{\mathrm{Rt}}| > 90$ deg are seen to induce an inflection in the C_{l_β} vs α slope before the wing with $\delta_{\mathrm{Rt}} = 0$ deg. This indicates earlier liftoff of the downstream tip vortex induced by the deflected winglet.

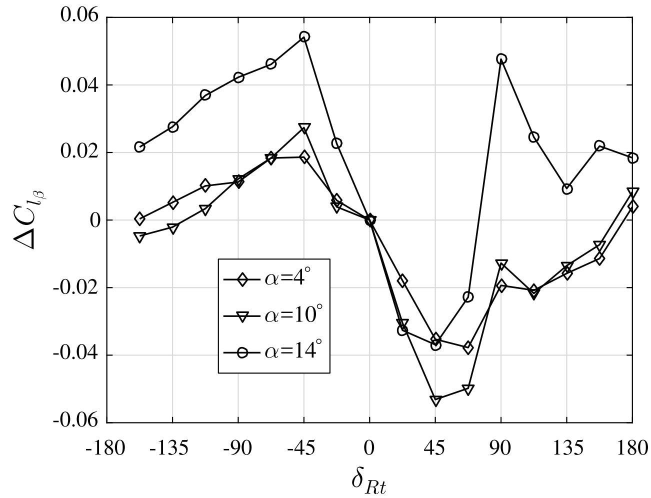

Fig. 12 Change in lateral stability derivative $\Delta C_{l_\beta} = C_{l_\beta}(\alpha, \delta_{\mathrm{Rt}}) - C_{l_\beta}(\alpha, \delta_{\mathrm{Rt}} = 0$ deg) as a function of right winglet deflection on aspect-ratio-one wings.

Of most interest for control purposes are the shallow deflection regions $|\delta_{\mathrm{Rt}}| < 90$ deg shown in Figs. 11b and 11c. In this region of deflections, shallow tip-up deflections reduce the magnitude of C_{l_β}, whereas shallow tip-down deflections increase the magnitude of C_{l_β}. Shallow tip-down deflections of 0 deg $> \delta_{\mathrm{Rt}} > -67.5$ deg, shown in Fig. 11c, are the only right tip winglet deflections to decrease the magnitude of C_{l_β}. When taken together, the region $|\delta_{\mathrm{Rt}}| < 90$ deg provides a means of manipulating C_{l_β} proportionally. Figure 12 shows the results of isolating the changes in C_{l_β} and plotting them as a function of right winglet deflections. This is shown for three different angles of attack in the liner region. At angles of attack in the linear region before roll stall, C_{l_β} is an antisymmetric function of winglet deflection in the shallow deflection regions. This effect may be considered as the result of lateral camber in which slight tip-down deflections of the right winglet $\delta_{\mathrm{Rt}} > 0$ deg result in a decrease in C_{l_β}, and $\delta_{\mathrm{Rt}} < 0$ deg increase C_{l_β}.

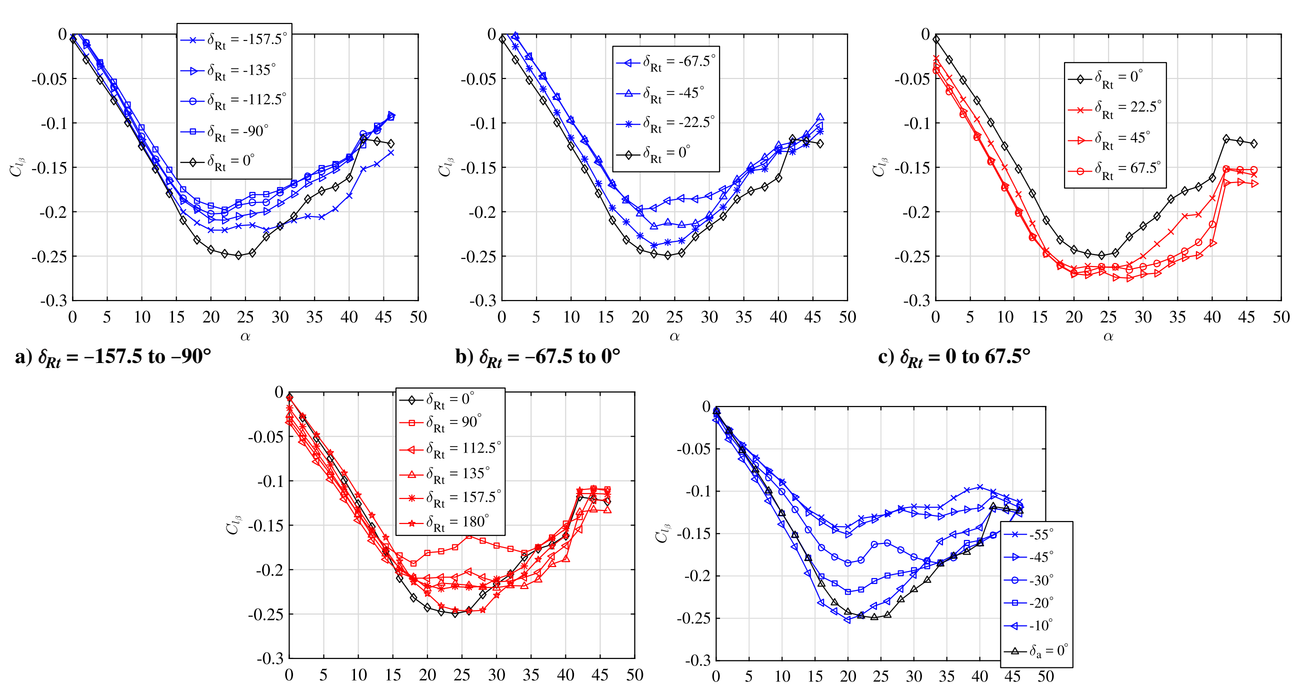

a) $\delta_{Rt} = -157.5$ to $-90°$ **b) $\delta_{Rt} = -67.5$ to $0°$** **c) $\delta_{Rt} = 0$ to $67.5°$**

d) $\delta_{Rt} = 90$ to $180°$ **e) Aileron $\delta_a = -55$ to $0°$**

Fig. 11 Stability derivative C_{l_β} as a function of angle of attack and control surface deflection. Both winglet and aileron models have an aspect ratio of one.

V. Winglet Tip Retraction Analogy

The deflection of an articulated winglet may be approximated as a wing tip retraction and a resulting change in wing aspect ratio. The roll moment generated by the deflection of one articulated winglet may be estimated by considering the lateral shift of the center of pressure of the wing by the effective retraction of the wing tip due to the cosine of the deflection angle. The right semispan is reduced by $b_w(1-\cos(\delta_{\mathrm{Rt}}))$ for $|\delta_{\mathrm{Rt}}| < 90$ deg and saturates to a reduction of b_w for $|\delta_{\mathrm{Rt}}| \geq 90$ deg. The modified wing span is then $b' = b - b_w(1-\cos(\delta_{\mathrm{Rt}}))$ before saturation and $b' = b - b_w$ after. The center of pressure is therefore shifted laterally by half the amount of the right wing tip retraction. The lift force then creates a moment about the geometric center of the wing with a moment arm half the length of the wing tip retraction. The lift itself is reduced because the effective wing aspect ratio, defined for rectangular wings simply as $AR = b/c$, is reduced to $AR' = b'/c$. Prandtl and Tietjens [21] first modeled this change in lift as an effective change in angle of attack α of the wing due to the increased downwash experienced by lower-aspect-ratio wings; the relationship is

$$\alpha' = \alpha - \frac{C_L(\alpha)}{\pi}\left(\frac{1}{AR'} - \frac{1}{AR}\right) \tag{1}$$

Although the preceding relationship is exact for wings with an elliptic lift distribution, Prandtl and Tietjens [21] found it to be satisfactory for rectangular planform wings as well. The value for lift may be realized by taking the original wings' lift versus angle-of-attack stability derivative C_{L_α} and multiplying it by the aspect ratio modified angle of attack. To close the model, we may use Prandtl and Tietjens's coefficient of lift, which is

$$C_L(\alpha') = \alpha' \frac{2\pi}{1 + (2/AR)} \tag{2}$$

The resulting change in roll moment induced by right tip winglet deflection is the modified lift crossed with the lateral shift of the center of pressure. This is written as

$$C_l(\alpha, \delta_{\mathrm{Rt}}) = \frac{C_L(\alpha')(b_w/2)(1-\cos(\delta_{\mathrm{Rt}}))}{b} \tag{3}$$

Here, b_w is the winglet span and b is the wing span. Figure 13 compares modeled lift and roll moment coefficients with measured data from a wing at zero sideslip. (Note that modeled data are shown in blue with dashed lines, measured data are in black with solid lines, and all data are differentiated by marker style for the angle of attack.) Not surprisingly, lift is underpredicted for high angles of attack as the low-aspect-ratio wing generates additional nonlinear lift past $\alpha = 15$ deg. This underprediction of lift does not lead to an underestimation of roll moment, however. The extreme angles of winglet deflection saturate to the roll moment predicted by removal of the winglet span from the wing, in which the analogy is satisfied identically. The estimated coefficient of roll captures the symmetric global behavior of roll moment generation but completely neglects the roll moment reversal generated by shallow tip-up deflections (-90 deg $< \delta < 0$ deg) at large angles of attack. The simple analogy of wing tip retraction considers only the symmetric shortening of the effective span. As was observed in the S-DPIV data, the winglet also affects a twist angle of the tip vortex system with respect to the wing. Therefore, a complete model will include consideration for both lateral and vertical changes in the tip vortex position.

VI. Conclusions

Flat-plate model wings with unity aspect ratios were experimentally tested over a set of α and β values with two different roll control mechanisms: rear aileron flaps, and articulated winglets. Aerodynamic loading data were measured using wind-tunnel testing on a microloading force balance, and the forces were nondimensionalized by the lifting body geometry. Near-wake flow imaging of the cross-stream plane captured the locations of the two tip vortices and illustrated their change in position as a function of sideslip and winglet deflection angles. The present study investigated the roll control authority produced by changing the cant angle of the right winglet independently of the left winglet, which was left planar with the wing. The articulated winglet was observed to show three distinct behaviors. First, globally, a variation of the winglet cant angle resulted in behavior identical to a retraction of the right wing tip. This was observed in the changes in the lift and roll moment. Second, shallow deflections of the winglet generated a roll moment by shifting the location of the right tip vortex higher above the wing with tip-up deflections and lower closer to the wing with tip-down deflections. This resulted in an angle between the two tip vortices and the wing and a roll moment. For shallow tip up ($\delta \approx -45$ deg), this twist angle was observed to mitigate or reverse the roll moment created by the tip retraction effect. Third, at non-zero sideslip, shallow deflections of the winglet behaved as lateral camber. Slight tip-down deflections increased right wing lateral camber and decreased C_{l_β}. These three effects were found to be generally superimposed on one another, although this is a gross over-simplification of low-aspect-ratio aerodynamics.

It was found that the articulated winglet control surfaces show promise as lateral control surfaces. Their roll control authority is comparable to standard flap control at large angles of attack. This is significant because low-aspect-ratio wings sustain lift to high angles of attack and conventional aileron surfaces show attenuated authority at high angles of attack. The winglet control authority is seen to linearly increase with angle of attack up to stall. The general monotonic increase of roll moment with angle of attack is due to increased circulation about the wing while one of the wing tips is effectively shortened, inducing spanwise asymmetry in lift. The notable exception to this behavior includes shallow negative (tip up) deflections at higher angles of attack in which a net negative roll moment is generated. A simple prediction of roll moment was found by looking at effective wing tip retraction and the resulting shift in the wings' center of pressure. This analogy's validity was tested for aspect-ratio-one wings with a span–winglet ratio of $b_w/b \approx 10\%$.

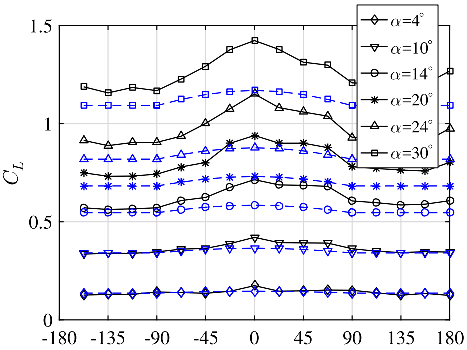

a) C_L as a function of δ_{Rt}

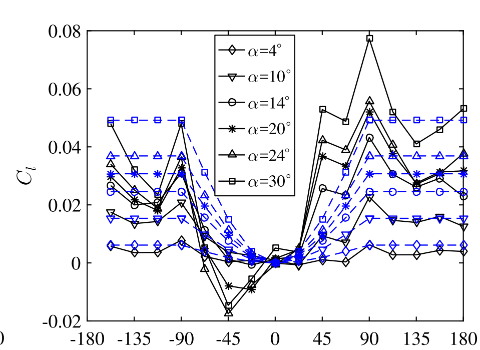

b) C_l as a function of δ_{Rt}

Fig. 13 Prediction of lift and roll moment considering asymmetric change in span by winglet deflection.

Near-wake flow imaging was conducted using a S-DPIV system in which both the tip vortices and the aft section of the LESR were imaged. Potential-like flow was seen to surround the tip vortices, and small areas of vorticity outlined the mean tip vortex core locations. The section of the near wake aft of the LESR was imaged as the peak TKE field, which also coincided with the wake velocity deficit region, and its lateral location is a function of sideslip. The right tip vortex position was manipulated by the winglet deflection such that the mean aerodynamic chord, or distance between the tip vortices, was reduced by winglet deflection. This follows the same trend as the lift and roll moment data and corroborates the tip retraction concept. The right tip vortex also followed the deflected winglet tip vertically. A complete model will account for both horizontal and vertical shifts of the tip vortex. Unsteadiness of the tip vortices was examined using instantaneous snapshots of the near wake. and the wandering path was presented as an ellipse. The downstream tip vortex in sideslip and the tip vortex behind deflected winglets were seen to be the most unsteady and had a preferred direction of wander.

Articulated winglets prove to be an effective means of manipulating the location of one of the dominant flow structures seen on low-aspect-ratio wings: the tip vortex. The maximum value of roll authority for the articulated winglet equates to a similar aileron flap deflection of 35 deg. Sideslip is shown to induce a much larger roll moment than the control authority of either aileron flap or winglet control surfaces. This results in some of the poor handling qualities of low-aspect-ratio and low inertia fliers in gusty environments. Deflections of the upstream winglet are most effective at directly mitigating the roll moment induced by sideslip, especially at higher angles of attack. Because articulated winglets affect the same roll-moment-generating mechanism as sideslip, the two effects scale together with the angle of attack. The data presented in this paper depict an initial study into aileron flap and articulated winglet control of canonical low-aspect-ratio wing models. From this set of data, further studies may be guided to explore the alternate location, size, and shape of the articulated winglet surfaces.

Acknowledgments

The authors are grateful for the partial support from the U.S. Air Force Office of Scientific Research and the U.S. Office of Naval Research, which made this study possible. The authors would like to thank Adam DeVoria for providing helpful comments and the three volumetric stereoscopic digital particle image velocimetry figures used in the Introduction.

References

[1] Phillips, W. F., *Mechanics of Flight*, 2nd ed., Wiley, New York, 2010.

[2] Etkin, B., and Reid, L. D., *Dynamics of Flight: Stability and Control*, 3rd ed., Wiley, Hoboken, NJ, 1996.

[3] Herbst, W., "Dynamics of Air Combat," *Journal of Aircraft*, Vol. 20, No. 7, 1983, pp. 594–598. doi:10.2514/3.44916

[4] Templin, R. J., "The Spectrum of Animal Flight: Insects to Pterosaurs," *Progress in Aerospace Sciences*, Vol. 36, Nos. 5–6, 2000, pp. 393–436. doi:10.1016/S0376-0421(00)00007-5

[5] Shields, M., and Mohseni, K., "Passive Mitigation of Roll Stall for Low Aspect Ratio Wings," *Advanced Robotics*, Vol. 27, No. 9, 2013, pp. 667–681. doi:10.1080/01691864.2013.778941

[6] Winter, H., "Flow Phenomena on Plates and Airfoils of Short Span," NACA, TM 798, July 1936.

[7] Pelletier, A., and Mueller, T. J., "Low Reynolds Number Aerodynamics of Low-Aspect-Ratio, Thin/Flat/Cambered-Plate Wings," *Journal of Aircraft*, Vol. 37, No. 5, 2000, pp. 825–832. doi:10.2514/2.2676

[8] Torres, G. E., and Mueller, T. J., "Low-Aspect-Ratio Wing Aerodynamics at Low Reynolds Numbers," *AIAA Journal*, Vol. 42, No. 5, 2004, pp. 865–873. doi:10.2514/1.439

[9] Grasmeyer, J. M., and Keennon, M. T., "Development of the Black Widow Micro Air Vehicle," *AIAA Aerospace Sciences Meeting and Exhibit*, AIAA Paper 2001-0127, 2001. doi:10.2514/6.2001-127

[10] Ifju, P. G., Jenkins, D. A., Ettinger, S., Lian, Y., Shyy, W., and Waszak, M. R., "Flexible-Wing-Based Micro Air Vehicles," *AIAA Aerospace Sciences Meeting and Exhibit*, AIAA Paper 2002-0705, 2002. doi:10.2514/6.2002-705

[11] Hassanalian, M., and Abdelkefi, A., "Classifications, Applications, and Design Challenges of Drones: A Review," *Progress in Aerospace Sciences*, Vol. 91, May 2017, pp. 99–131. doi:10.1016/j.paerosci.2017.04.003.

[12] Watkins, S., Milbank, J., Loxton, B. J., and Melbourne, W. H., "Atmospheric Winds and Their Implications for Micro Air Vehicles," *AIAA Journal*, Vol. 44, No. 11, 2006, pp. 2591–2600. doi:10.2514/1.22670

[13] Taira, K., and Colonius, T., "Three-Dimensional Flows Around Low-Aspect-Ratio Flat-Plate Wings at Low Reynolds Numbers," *Journal of Fluid Mechanics*, Vol. 623, March 2009, pp. 187–207. doi:10.1017/S0022112008005314

[14] Yilmaz, T. O., and Rockwell, D., "Three-Dimensional Flow Structure on a Maneuvering Wing," *Experiments in Fluids*, Vol. 48, No. 3, 2010, pp. 539–544. doi:10.1007/s00348-009-0772-9

[15] Shields, M., and Mohseni, K., "Roll Stall for Low-Aspect-Ratio Wings," *Journal of Aircraft*, Vol. 50, No. 4, 2013, pp. 1060–1069; also, erratum, Vol. 53, No. 4, 2016, pp. 1186–1188. doi:10.2514/1.C031933

[16] DeVoria, A. C., and Mohseni, K., "A Vortex Model for Forces and Moments on Low-Aspect-Ratio Wings in Side-Slip with Experimental Validation," *Proceedings of the Royal Society of London, Series A: Mathematical and Physical Sciences*, Vol. 473, No. 2198, 2017, pp. 5–7. doi:10.1098/rspa.2016.0760

[17] Linehan, T., and Mohseni, K., "Leading-Edge Flow Reattachment and the Lateral Static Stability of Low-Aspect-Ratio Rectangular Wings," *Physical Review Fluids*, Vol. 2, No. 11, 2017, Paper 113901. doi:10.1103/PhysRevFluids.2.113901

[18] Etkin, B., *Dynamics of Atmospheric Flight*, 1st ed., Dover, Mineola, NY, 1972, pp. 304–306.

[19] DeVoria, A. C., and Mohseni, K., "On the Mechanism of High-Incidence Lift Generation for Steadily Translating Low-Aspect-Ratio Wings," *Journal of Fluid Mechanics*, Vol. 813, Feb. 2017, pp. 110–126. doi:10.1017/jfm.2016.849

[20] Shields, M., and Mohseni, K., "Inherent Stability Modes of Low Aspect Ratio Wings," *Journal of Aircraft*, Vol. 52, No. 1, 2015, pp. 141–155. doi:10.2514/1.C032636

[21] Prandtl, L., and Tietjens, O. G., *Applied Hydro- and Aeromechanics*, 1st ed., McGraw-Hill, York, PA, 1934, pp. 144–225.

[22] Drela, M., *Flight Vehicle Aerodynamics*, MIT Press, Cambridge, MA, 2014, pp. 99–122.

[23] Glauert, H., "Theoretical Relationships for an Aerofoil with Hinged Flap," *British ARC*, No. 1095, 1927.

[24] Milne-Thomson, L. M., *Theoretical Aerodynamics*, Dover, Mineola, NY, 1958, p. 197.

[25] Fischel, J., Naeseth, R. L., Hagerman, J. R., and O'Hare, W. M., "Effect of Aspect Ratio on the Low-Speed Lateral Control Characteristics of Untapered Low-Aspect-Ratio Wings Equipped with Flap and with Retractable Ailerons," NASA Langley Research Center TR-1091, Hampton, VA, Jan. 1952.

[26] Whitcomb, R. T., "A Design Approach and Selected Wind-Tunnel Results at High Subsonic Speeds for Wing-Tip Mounted Winglets," NASA Langley Research Center TN-D-8260, Hampton, VA, 1976, https://ntrs.nasa.gov/search.jsp?R=19760019075 [retrieved 2018].

[27] Kroo, I., "Drag due to Lift: Concepts for Prediction and Reduction," *Annual Review of Fluid Mechanics*, Vol. 33, No. 1, 2001, pp. 587–617. doi:10.1146/annurev.fluid.33.1.587

[28] McGowan, A. R., Cox, D., Lazos, B., Waszak, M., Raney, D., Siochi, E., and Pao, S., "Biologically Inspired Technologies in NASA's Morphing Project," *Proceedings of SPIE*, Vol. 5051, July 2003, pp. 1–13. doi:10.1117/12.484714

[29] Beechook, A., and Wang, J., "Aerodynamic Analysis of Variable Cant Angle Winglets for Improved Aircraft Performance," *2013 19th International Conference on Automation and Computing*, IEEE Publ., Piscataway, NJ, 2013, pp. 1–6, http://ieeexplore.ieee.org/document/6662041/ [retrieved 2018].

[30] Wolowicz, C., and Yancey, R., "Summary of Stability and Control Characteristics of the XB-70 Airplane," NASA TM-X-2933, Edwards AFB, CA, Oct. 1972.

[31] Oduyela, A., and Slegers, N., "Gust Mitigation of Micro Air Vehicles Using Passive Articulated Wings," *Scientific World Journal*, Vol. 2014, Jan. 2014, Paper 598523. doi:10.1155/2014/598523

[32] Leylek, E., and Costello, M., "Use of Compliant Hinges to Tailor Flight Dynamics of Unmanned Aircraft," *Journal of Aircraft*, Vol. 52, No. 5, 2015, pp. 1692–1706.
doi:10.2514/1.C033056

[33] Bourdin, P., Gatto, A., and Friswell, M. I., "Aircraft Control via Variable Cant-Angle Winglets," *Journal of Aircraft*, Vol. 45, No. 2, 2008, pp. 414–423.
doi:10.2514/1.27720

[34] Bourdin, P., Gatto, A., and Friswell, M. I., "Experimental Investigation into Articulated Winglet Effects on Flying Wing Surface Pressure Aerodynamics," *Journal of Aircraft*, Vol. 47, No. 5, 2010, pp. 1811–1815.
doi:10.2514/1.C000251

[35] Hoey, R., "Research on the Stability and Control of Soaring Birds," *28th National Heat Transfer Conference*, AIAA Paper 1992-4122, 1992, pp. 393–406.
doi:10.2514/6.1992-4122

[36] Bryan, G. H., *Stability in Aviation: An Introduction to Dynamical Stability as Applied to the Motions of Aeroplanes*, 1st ed., Macmillan, London, 1911, p. 20.

[37] Shields, M., and Mohseni, K., "Effects of Sideslip on the Aerodynamics of Low Aspect Ratio Wings at Low Reynolds Numbers," *AIAA Journal*, Vol. 50, No. 1, 2012, pp. 85–99.
doi:10.2514/1.J051151

[38] "Calibration and Use of Internal Strain-Gage Balances with Application to Wind Tunnel Testing," *Recommended Practice, AIAA Standards*, R-091-2003, Reston, VA, 2003.

[39] Soloff, S. M., Adrian, R. J., and Liu, Z. C., "Distortion Compensation for Generalized Stereoscopic Particle Image Velocimetry," *Measurement Science and Technology*, Vol. 8, No. 12, 1997, pp. 1441–1454.
doi:10.1088/0957-0233/8/12/008

[40] Wieneke, B., "Stereo-PIV Using Self-Calibration on Particle Images," *Experiments in Fluids*, Vol. 39, No. 2, 2005, pp. 267–280.
doi:10.1007/s00348-005-0962-z

[41] Raffel, M., Willert, C. E., and Kompenhans, J., *Particle Image Velocimetry*, Springer–Verlag, New York, 1998, pp. 209–239.

[42] Graftieaux, L., Michard, M., and Grosjean, N., "Combining PIV, POD and Vortex Identification Algorithms for the Study of Unsteady Turbulent Swirling Flows," *Measurement Science and Technology*, Vol. 12, No. 9, 2001, pp. 1422–1429.
doi:10.1088/0957-0233/12/9/307

[43] Kaplan, S. M., Altman, A., and Ol, M., "Wake Vorticity Measurements for Low-Aspect-Ratio Wings at Low Reynolds Number," *Journal of Aircraft*, Vol. 44, No. 1, 2007, pp. 241–251.
doi:10.2514/1.23096

[44] Leweke, T., and Williamson, C. H. K., "Cooperative Instability of a Vortex Pair," *Journal of Fluid Mechanics*, Vol. 360, April 1998, pp. 85–119.
doi:10.1017/S0022112097008331

[45] Crowe, S. C., "Stability Theory for a Pair of Trailing Vortices," *AIAA Journal*, Vol. 8, No. 12, 1970, pp. 2172–2179.
doi:10.2514/3.6083